Electron microscopy of reaction layers between SiC and Ti-6Al- 4V after laser embedding

Kloosterman, A.B; Kooi, B.J.; de Hosson, J.T.M.

Published in:
Acta Materialia

DOI:
10.1016/S1359-6454(98)00265-1

Publication date:
1998

Pergamon

Acta mater. Vol. 46, No. 17, pp. 6205–6217, 1998

Printed in Great Britain
PII: S1359-6454(98)00265-1
1359-6454/98 $19.00 + 0.00

ELECTRON MICROSCOPY OF REACTION LAYERS BETWEEN SiC AND Ti–6Al–4V AFTER LASER EMBEDDING

A. B. KLOOSTERMAN, B. J. KOOI and J. TH. M. DE HOSSON†

Department of Applied Physics, The Netherlands Institute for Metals Research and Materials Science Centre, University of Groningen, Nijenborgh 4, 9747 AG Groningen, The Netherlands

(Received 12 May 1998; accepted 10 July 1998)

Abstract—A detailed electron microscopic examination of the interface between Ti and SiC is concentrated on. The metal–matrix-composites (MMCs) are produced by the laser particle injection processing route. SiC particles are entrapped during solidification of liquid Ti. Since the injected particles partially dissolve, depending on the process conditions, new phases are formed in the matrix. The degree of dissolution will significantly influence the mechanical performance of the MMC. In particular, the interfacial region with the various phases between Ti and SiC particles is closely investigated with (high resolution) transmission electron microscopy. Furthermore, hardness indents are performed to examine the crack initiation and the crack propagation behaviour at the interface. © *1998 Acta Metallurgica Inc. Published by Elsevier Science Ltd. All rights reserved.*

1. INTRODUCTION

The combination of many excellent material properties results in a widespread application of titanium. The request for specific demands is satisfied by the versatile range of titanium alloys. The two main virtues of titanium are the unique strength to weight ratio and the good corrosion resistance. Further, titanium has a high melting temperature and can be used at temperatures up to ~550° with good fatigue, creep and toughness properties. At present, the main applications lie in the aerospace and steam turbine industry, but it is expected that the use of titanium will expand to other fields. This breakthrough will depend on the progress made in circumventing the disadvantages of titanium, namely its high friction and poor wear properties. This difficulty can be tackled by applying a protective coating.

Several experimental methods can be applied for the production of a protective coating with high power lasers. In the case of laser embedding, two different processes can be used. The first method is to pre-deposit the powder on the substrate [1]. The disadvantage is that the laser beam does not initially interact with the substrate material, but with the powder particles. In order to melt the substrate material, the heat has to be transported through the powder layer, which might result in the melting of the powder. Depending on thermophysical properties, new phases will grow from the melt which do not necessarily correspond with the original addition. The second method is the particle injection process during laser treatment [2–5]. Here, the laser beam primarily interacts with the substrate and to a lesser extent with the particles. The resulting microstructure is determined by several parameters, namely the positioning of the powder flow, the particle size, the particle velocity, and the amount of powder. Therefore, the relevance of these different parameters will be examined.

In this study, SiC particles are injected during laser melting of Ti–6Al–4V. The process of particle injection during laser processing is examined and appears to be very sensitive for small deviations in the amount of powder, the particle velocity and the positioning of the particle flow. Further the microstructural features of the various coatings are examined. In the case of SiC, the reactivity of titanium and the decomposition of SiC results in the formation of various phases. The phases are identified with transmission electron microscopy (TEM), whereas the composition is determined by energy dispersive X-ray analysis (EDX).

2. EXPERIMENTAL PROCEDURES

The experiments were carried out with the use of a continuous wave 2 kW Rofin Sinar Nd:YAG laser. The laser beam is guided by an optical fibre with a diameter of 0.8 mm, which is also the minimum spot size. For the experiments the beam diameter amounted to ~2–3 mm. The applied laser power was 1000 W and the scan velocities were in the range of 8–17 mm/s. Argon shielding gas was applied to prevent oxidation of the substrate. SiC

†To whom all correspondence should be addressed.

particles were injected, with a particle size between 60 and 100 μm. Despite the fact that spherical SiC particles would be preferable, quite acute SiC particles were injected. The powder was supplied by a powder feeding apparatus (Metco 9MP). The applied powder feed was varied between 17 and 50 mg/s, with a deviation of ± 3 mg/s. The carrier flow amounted to 0.08 l/s. To get rid of the carrier flow, the powder was fed through a cyclone in which the carrier gas was removed by the carrier gas outlet. Ti–6Al–4V was used as the substrate material. The dimensions of the specimens were 40 mm in diameter and 5 mm in thickness. Before processing, the specimens were sand blasted to increase the absorption of the laser beam. Subsequently, they were ultrasonically cleaned.

After laser treatment cross sections were made by embedding the material followed by several polishing steps. Finally, the cross sections were chemically etched in a solution of 0.3% HF and 1% HNO_3 in demineralized water. The microstructure was examined with a Philips XL-30 FEG scanning electron microscope, equipped with an Energy Dispersive X-ray detector (EDX) and the Electron Backscatter Diffraction (EBSD) technique. Subsequently, a JEOL-4000EX/II transmission electron microscope was used to determine the different phases present in the meltpool. For mechanical testing, hardness measurements were performed with a Vickers hardness indenter.

Electron backscattering diffraction involves the formation of diffraction patterns in a manner first described by Kikuchi in 1928. Kikuchi accounted the phenomenon to occur for electrons transmitting a thin crystal. The EBSD analysis makes use of a different geometry since the electrons are backscattered instead of being transmitted. Still the same explanation is valid for the appearance of Kikuchi patterns [6, 7]. The specimen detector geometry corresponds to the Philips integrated EBSD system. The electrons coming from above impinge on the specimen under an angle of 70°. The phosphor screen with a diameter of 45 mm is positioned on the right, with a minimum distance of ~20 mm, ensuring a solid angle exceeding 90°. Furthermore, the distance from phosphorous screen to specimen can be changed. Behind the phosphorous screen a camera is mounted to record the pattern. The patterns are imaged with the use of a computer monitor, in which they are subsequently adapted in order to increase the image quality.

In fact, the symmetry of the EBSD pattern is a two-dimensional projection of the symmetry in three dimensions of the atomic arrangement within a crystal. Therefore, the obtained backscatter pattern contains crystallographic information concerning the crystal structure and the orientation of the analysed crystal. With the use of the Crystal Orientation Software (COS) it is possible to simulate the pattern obtained. In order to translate the orientations obtained to the specimen, the COS software provides a transformation matrix which relates the crystallographic direction to the specimen directions. This can be depicted by pole figure projections.

3. PARTICLE INJECTION PROCESS

Based on the model proposed by Rosenthal [8], temperature profiles are calculated to get an estimate of the shape of the meltpool in the direction of the laser beam. The calculations are performed for a laser beam with a homogeneous temperature distribution and Ti–6Al–4V was taken as the substrate material. The analytical model did not incorporate either melting or convection. From these calculations it appeared that: (i) the highest temperature is situated behind the middle of the laser beam and (ii) the meltpool is extended behind the laser beam. Actually, this means that the dissolution of the particles can be controlled by the positioning of the powder flow as depicted in Fig. 1. Situation A will result in much more dissolution of the powder than B which is caused by the longer time spent in the meltpool. For the second case, some particles do not even cross the laser beam anymore, which

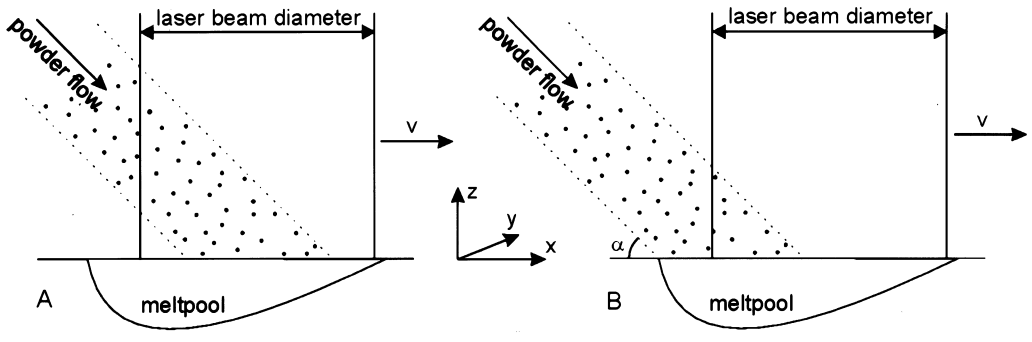

Fig. 1. Illustration of the powder flow positioning during laser treatment (A) aligned at the centre of the laser beam, (B) aligned at the back of the laser beam.

might result in a considerable increase of the temperature.

Besides the positioning, the interaction time of the SiC particles with the laser is also determined by the particle velocity. Although the interaction time is in the order of milliseconds, there is a considerable increase in temperature due to the high absorption of SiC particles (~90%) at a wavelength of 1.06 μm. Furthermore, the particle size also influences the temperature increase by its surface/volume ratio. The optimum injection velocity is found to be ~1.2 m/s, resulting in a temperature increase of ~2000°C in the case of a SiC particle with a diameter of 80 μm, injected in the centre of the laser beam. The temperature is assumed to increase homogeneously through the particle and gas cooling is neglected. If relatively small dissolution with respect to the particle size is desired, large particles should be used. Another requirement is that the particle velocity should be large enough to reach the bottom of the meltpool. Note that the angle α should be large enough to prevent rebounding.

In the case of SiC injection an increase in the amount of particles results in a higher total absorbed laser intensity. As a consequence the dimensions of the meltpool will increase. However, too much powder may lead to cladding of SiC particles onto the substrate which yields a very rough laser track and shields the substrate from the laser radiation.

4. ELECTRON MIRCOSCOPY CHARACTERIZATION

By changing the position of the particle flow from behind to beyond the centre of the laser beam, there is a transition from modest dissolution to considerable dissolution of SiC particles. For the latter case this results in a meltpool filled with reaction products of Ti with Si and C. The following microstructural description applies to the situation where the particles are injected somewhat behind the middle of the laser beam. However, by changing the particle injection position, the presence and amount of the different microstructures can be controlled. Figure 2 shows the cross section of a laser track with embedded SiC particles. The depth of the laser track amounts to ~0.5 mm. The particles are homogeneously distributed over the meltpool, where the volume increase due to the addition of SiC amounts to 10–15%. First, the change of microstructural composition of the matrix will be described. Second, the appearance of the reaction layer around the SiC particles, which is present under all injection conditions, will be studied in more detail. Conclusions concerning the phases present in the meltpool are mainly based on the combination of XRD measurements and EDX analysis, where in some specific cases TEM is used.

4.1. Matrix

As the SiC particles partially dissolve, the matrix composition changes. The matrix consists of various phases, where the percentage of each gradually changes as a function of depth. Figure 3 shows the structure near the bottom of the laser track. A eutectic structure is observed which surrounds grains of alloyed titanium. These Ti grains contain the alloying elements Al, V and Si and exhibit a lenticular martensitic structure. The eutectic lamellae consist of alternating Ti and Ti_5Si_3 layers. This observation corresponds to the binary phase diagram of Ti and Si, since a eutectic is present at 13.7 at.% Si. Thus the solidification starts with the formation of Ti grains followed by eutectic solidification. In the middle of the laser track TiC dendrites are randomly oriented and distributed over

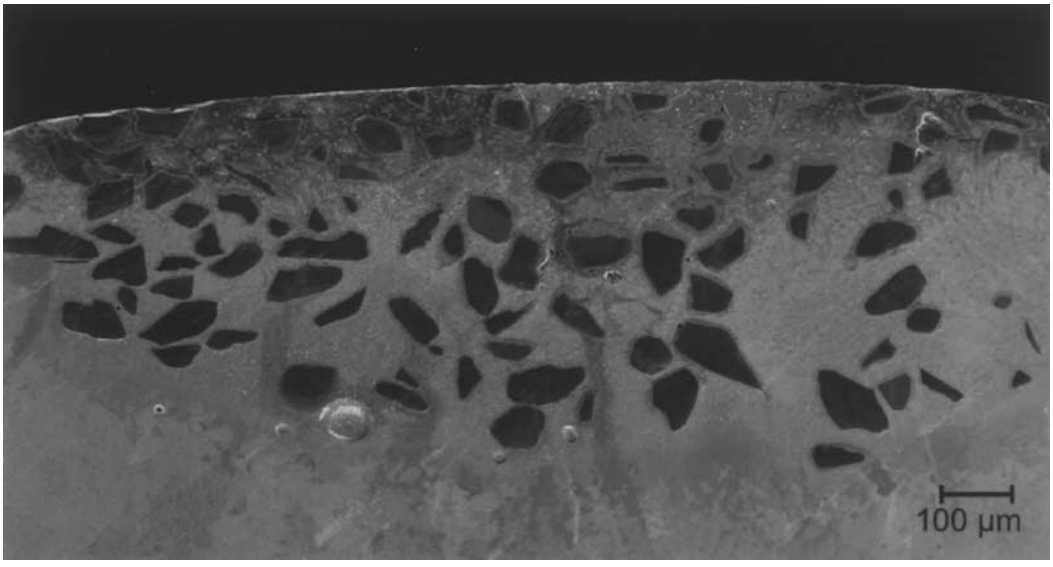

Fig. 2. SEM micrograph of the cross section showing SiC particles embedded in a Ti–6Al–4V matrix.

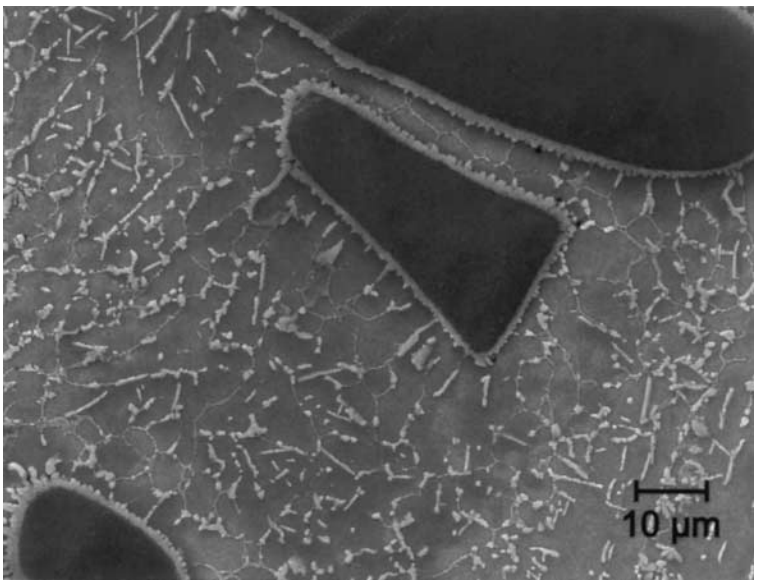

Fig. 3. SEM micrograph of the structure at the bottom of the laser track showing SiC particles surrounded by a TiC reaction layer. The matrix consists of Ti–6Al–4V grains (dark) surrounded by a eutectic structure (white).

the laser track, as shown in Fig. 4. This indicates that a reasonable amount of carbon is dissolved in the melt for this region. Furthermore, the amount of eutectic structure is increased. Near the top of the meltpool faceted Ti_5Si_3 grains (Fig. 5) are situated, where the angles between the facets point to a hexagonal phase of Ti_5Si_3. In addition this region also contains a small amount of eutectic structure and TiC dendrites.

With TEM, we looked in more detail at the matrix in the upper part of the meltpool. Several Ti_5Si_3 grains with a size of approximately 0.6 μm are observed, as depicted in Fig. 6. The black particle in the image corresponds to a Ti_5Si_3 grain which is oriented along its [0001] pole with $d_{\{10\bar{1}0\}}$ of 0.645 nm. In comparison with SEM observations these Ti_5Si_3 grains are differently shaped and have different dimensions. Therefore, these grains are expected to be part of the eutectic structure. In between these grains Ti needles are observed. Roughly, the Ti_5Si_3 particles seem to be spherical, but a closer look reveals many facets.

As already mentioned, the microstructure can be controlled by changing the injection position. The laser particle injection process is performed for six different injection positions, starting from the

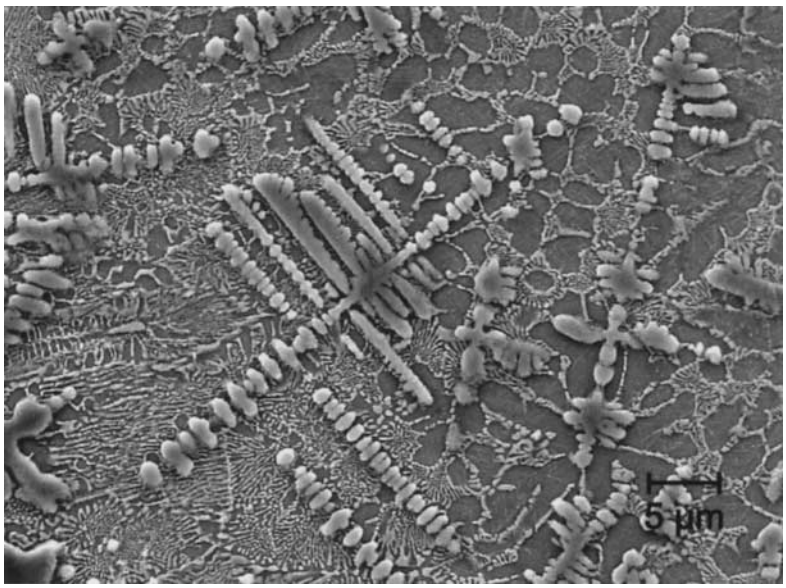

Fig. 4. SEM micrograph of the structure at the middle of the laser track showing TiC dendrites and a large portion of eutectic structure.

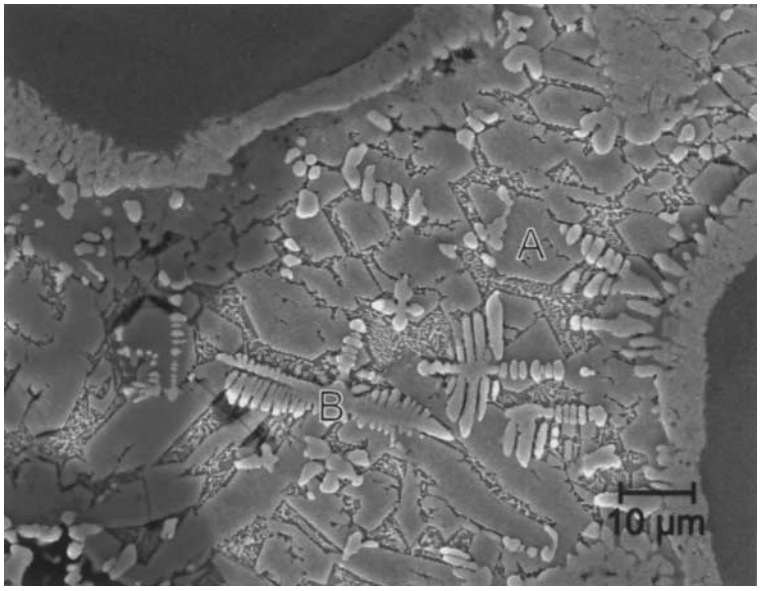

Fig. 5. SEM micrograph of the structure at the top of the laser track showing SiC particles surrounded by a TiC reaction layer. The matrix consists of strongly faceted Ti_5Si_3 grains (A) and TiC dendrites (B).

middle, with step sizes of 0.3 mm towards the back of the laser beam (negative x-direction). All other laser parameters were kept constant. In the case of particle injection in the centre of the laser beam, the microstructure contains regions at the top of the track which almost completely consists of Ti_5Si_3 and TiC cells. On the other hand it is found that the last laser track mainly consists of Ti grains surrounded by the eutectic structure, as shown in Fig. 3. The intermediate laser injection position exhibits a smooth transition between these extremes. Similar effects of the different degree of dissolution can be obtained by increasing the scan velocity [9]. However, the laser power has to be

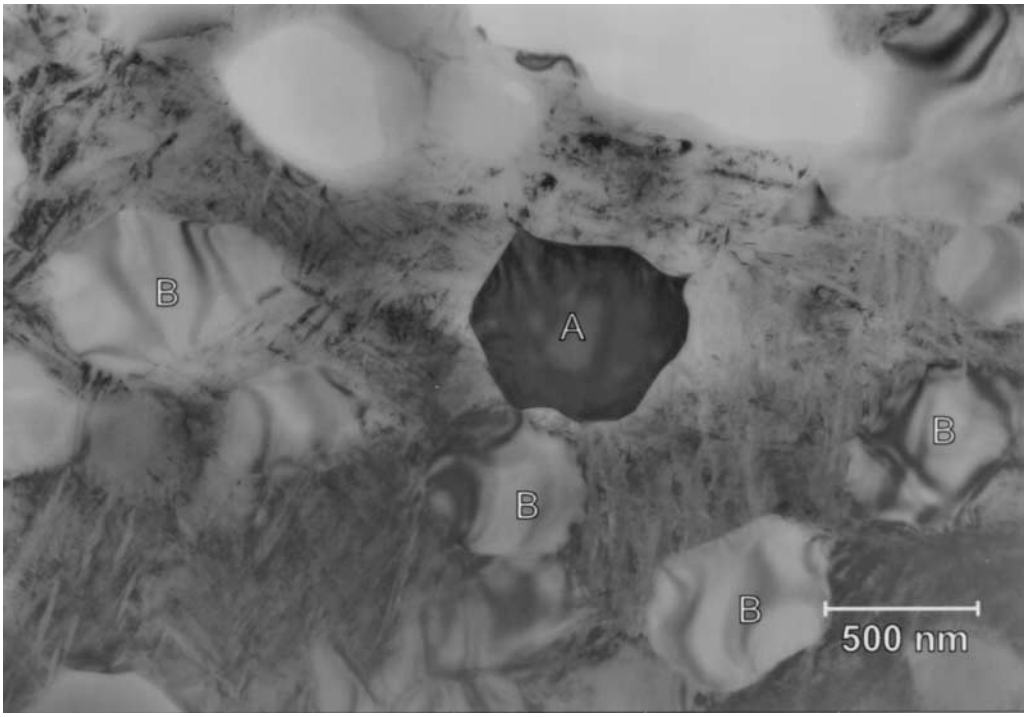

Fig. 6. Bright field TEM micrograph of the eutectic structure showing a strongly diffracting Ti_5Si_3 grain (A) and differently oriented Ti_5Si_3 grains (B). The structure in between consists of Ti needles.

increased to obtain the same track depth, which will increase the absorbed power by the SiC particles.

Hardness measurements are performed to determine the hardness of the different phases present in the laser track with SiC particles. The hardness of the substrate material Ti–6Al–4V amounts to 350 HV. The heat affected zone below the laser track exhibits an increase in hardness up to 400 HV. It must be mentioned that all other hardness indents are performed at composite structures. The hardness of the structure consisting of Ti grains surrounded by the eutectic structure, depicted in Fig. 3, is measured to be ~650 HV. This value increases with decreasing Ti grain size. The areas which mainly consist of Ti_5Si_3 exhibit a hardness of 1100 HV. However, this value can be influenced by the presence of TiC cells and dendrites. As the composition of the matrix changes with the particle injection position, it is possible to control the average matrix hardness in the range between 650 and 1100 HV. It is anticipated that the lowest value is preferable with respect to its ductile behaviour.

4.2. Reaction layer

The injected SiC particles are always surrounded by a reaction layer. At high temperatures, the SiC decomposes while both components form a new phase with Ti. With increasing reaction time or temperature, the thickness of the layer will increase, which results simultaneously in a decrease of the diameter of the remaining SiC particles. EBSD and EDX analysis indicate that the reaction layer mainly consists of TiC. In the case of TiN and TiC particle injection, there is no reaction layer present. The melting of these particles only results in the formation of TiC and TiN dendrites in the environment of the particle.

The reaction layer of TiC around the SiC particles is of special interest because it will determine the mechanical properties of the metal–matrix-composite (MMC), which will be described in Section 5. In principle, the reaction layer appears in two different ways, namely a cellular reaction layer and an irregular reaction layer, which can be observed in Figs 3 and 5, respectively. The cellular reaction layer is relatively thin and very regularly shaped all around the particle. Furthermore, the layer is often well connected to the particle and exhibits minor porosity.

In order to obtain crystallographic information, the reaction layer is examined with the use of EBSD. This is shown in Fig. 7, where the four EBSD patterns represent the orientation of the reaction layer at each side of a SiC particle. Along each side of a cellular reaction layer the pattern remains unchanged. Furthermore, a three-dimensional representation is given of the ⟨100⟩ directions with respect to the specimen axis. Although it is not known under which angle of inclination the surface of SiC is oriented, it is found that the cellular type of reaction layer always grows in the ⟨100⟩ direction nearly perpendicular to the SiC surface. The remaining ⟨100⟩ directions might give an indication of the angle of inclination of the sides of the SiC particle. A specific relation is not found between the orientation of SiC and the TiC reaction layers. Therefore, the preferred orientation of TiC is a growth phenomenon related to the steepest thermal gradient, as the thermal conductivity of TiC is maximum in the [100] direction. The three-dimensional representation exhibits only a slight change in orientation between the [100] direction perpendicular to the surface of grains B and C.

Examination of the irregular reaction layer with EBSD indicates that the reaction layer consists of TiC grains which are randomly oriented. In contrast to the cellular type, this type of layer is relatively thick. In addition large pore volumes are observed within the reaction layer, which can partially be explained by the volume decrease of ~5% as a consequence of the formation of TiC. However, this only becomes important for solid state reactions. Sometimes, cracks arise in the thick reaction layers as a consequence of thermal stresses.

In order to study this type of reaction layer in more detail, CTEM and HRTEM examinations were carried out. Electron diffraction analysis of the irregular reaction layer reveals the presence of another phase, namely Ti_3SiC_2. Although the symmetry in the diffraction pattern of Ti_3SiC_2 and 6H-SiC is equal, the *c*-lattice constant differs significantly (1.764 nm vs 1.509 nm) [10]. Figure 8 depicts an atomic resolution image of Ti_3SiC_2 obtained by means of HRTEM, in which the inset shows the simulated pattern which is in good agreement. The atomic configuration of Ti_3SiC_2 exhibits the 8H-like structure. The ternary phase is found to be present as small plates around the spherical and randomly oriented TiC grains, as shown in Fig. 9. In the literature, similar structures are observed for TiC and Ti_3SiC_2, obtained with a specific sintering process [11]. In most cases, a specific orientation relationship between the TiC grains and plates of Ti_3SiC_2 is not observed. However, for one specific situation an orientation relation appeared to be present between TiC and Ti_3SiC_2. This is shown in Fig. 10(A) in which a Ti_3SiC_2 plate is connected to a relatively large, spherical TiC grain, both being simultaneously viewed along a low-index zone axis. The TiC and Ti_3SiC_2 are viewed along the ⟨110⟩ and $\langle 11\bar{2}0\rangle$, respectively. Based on chemical and geometrical considerations, the lowest interfacial energy occurs if the basal plane of Ti_3SiC_2 is parallel to the (111) of TiC. TiC(111) consists of alternating closed packed planes of either Ti or C atoms, which are identical to the fully Ti or C basal planes as stacked in Ti_3SiC_2. Therefore, it is remarkable that the basal planes of Ti_3SiC_2 are found to be aligned parallel to the elongated direc-

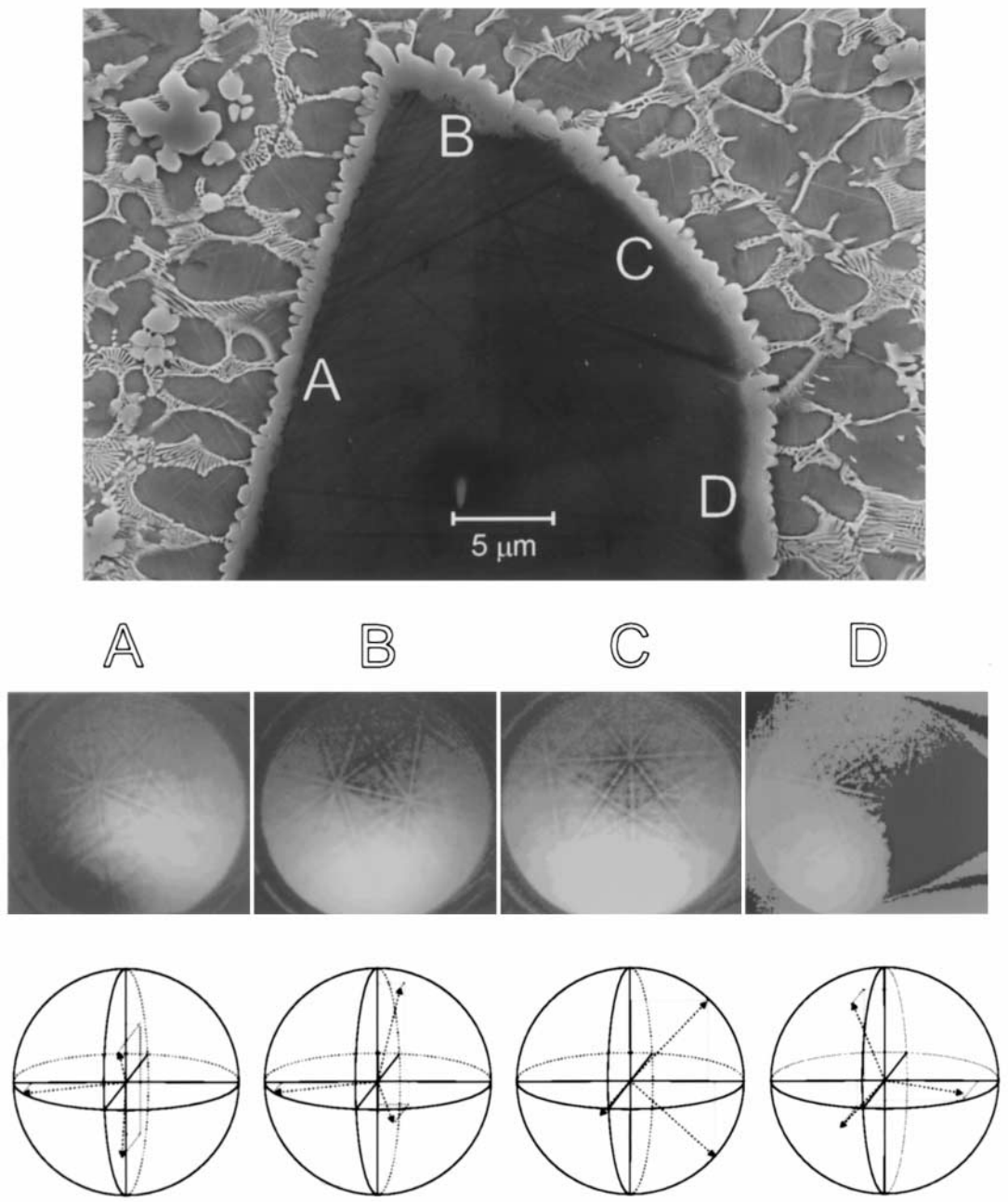

Fig. 7. SEM micrograph showing a TiC reaction layer around a SiC particle. EBSD measurements are performed at the four sides A, B, C and D of the reaction layer. The corresponding backscatter Kikuchi patterns are shown in the middle. Below the three-dimensional projection of the crystallographic ⟨100⟩ directions of TiC are given relative to the specimen axis.

tion of the plate, which implies the latter mentioned stacking does not occur. The TiC{111} and Ti_3SiC_2{0001} are found to be rotated over $5^\circ \pm 0.5^\circ$, with respect to each other. Instead, two other planes are found to be more or less parallel, i.e. the $\_\{111\}_{TiC}//\{10\bar{1}3\}_{Ti_3SiC_2}$ and the $\{002\}_{TiC}//\{10\bar{1}4\}_{Ti_3SiC_2}$. An obvious reason for the parallelism of these planes is not found, also because the image does not reveal a clear and sharp interface. The reason for the orientation of the basal planes parallel to the surface of the plates and approximately perpendicular to the (macroscopic) surface of the TiC grain, might be the lower surface free energy of the close packed plane. However, it is anticipated that a more probable, but not independent reason is the growth direction during solidification. In that case the grains grow away from the TiC surface along the basal planes since these planes are probably the fastest growing. In Fig. 10(B) an adjacent Ti_3SiC_2 plate is tilted in a

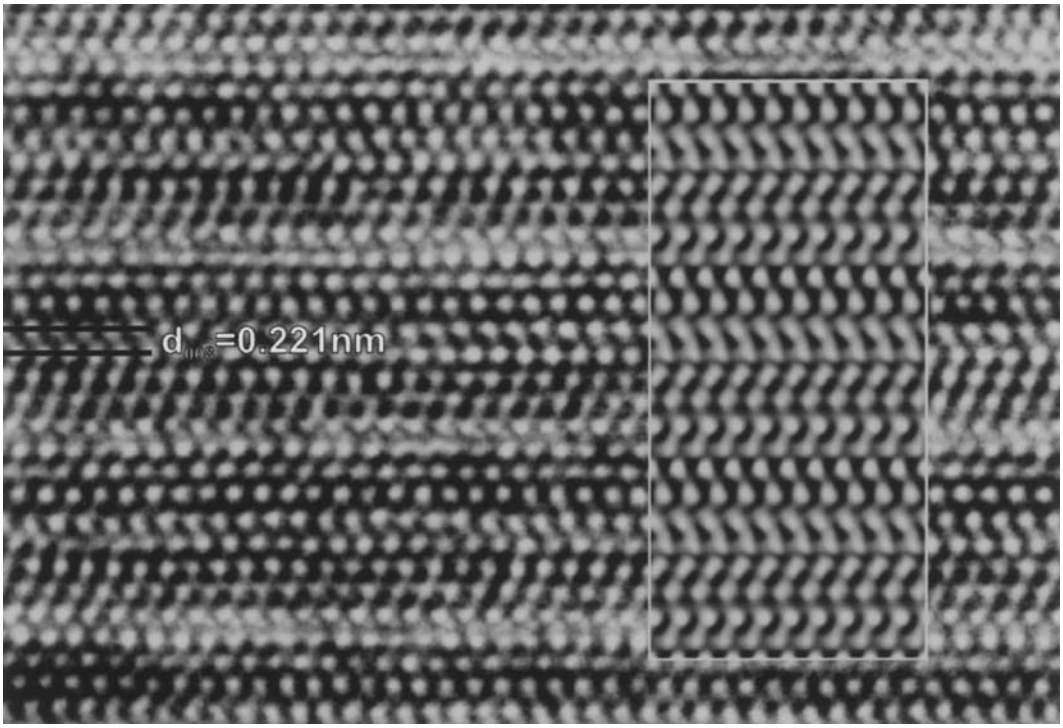

Fig. 8. HRTEM image showing the atomic structure of Ti_3SiC_2 viewed along ⟨1120⟩. The inset depicts the simulated structure.

strong diffraction condition. It can be seen that the TiC grain contains stacking faults, on two sets of slightly inclined {111} planes. Furthermore, the former Ti_3SiC_2 grain, on the left-hand side, exhibits a stacking fault being situated on the basal plane. It would be interesting to know how the stacking fault

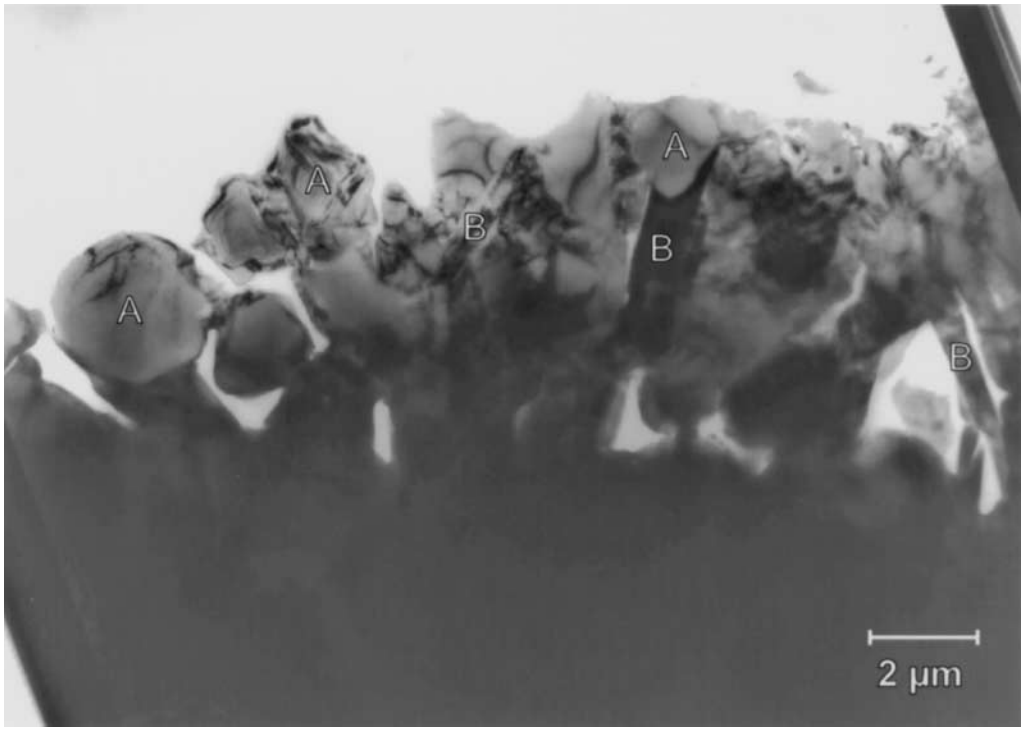

Fig. 9. Bright field TEM micrograph of the reaction layer around SiC consisting of round TiC grains (A) and plate like structures of Ti_3SiC_2 (B).

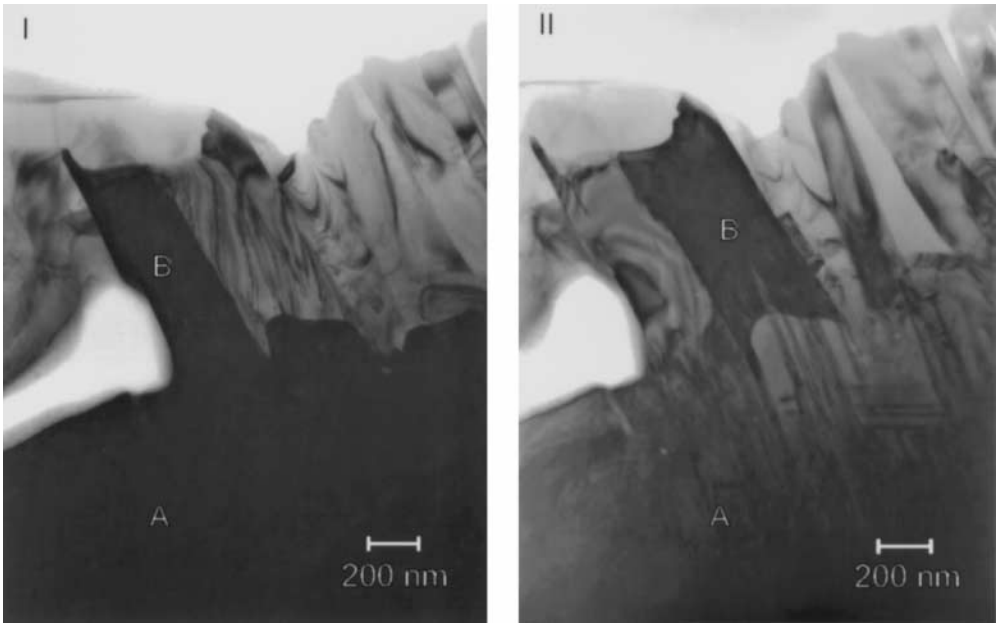

Fig. 10. TEM micrographs of TiC grains (A) with adjacent plates of Ti_3SiC_2 (B), (I) both strongly diffracting, (II) Ti_3SiC_2 plate strongly diffracting. Stacking faults are visible in TiC.

occurs with respect to the chemical composition of the basal planes in the crystal structure, in particular with regard to the possibility of Ti_3SiC_2 deforming plastically [12].

Although all different phases in the laser track are known, the solidification route is hard to determine because of both the absence of the ternary phase diagram over the complete temperature range and the non-equilibrium conditions. Nevertheless, it is possible to relate a certain area in the ternary phase diagram [13], depicted in Fig. 11, to a specific microstructural region in the meltpool. Additional information concerning the temperature can be derived from the binary phase diagrams. In principle we start from the condition in which only SiC and Ti are present, if we neglect the alloying elements. After partial decomposition or melting of SiC, the solidification starts with the formation of the reaction layer. This situation corresponds with the region within the triangle in the Ti–Si–C phase diagram formed by TiC, SiC and Ti_3SiC_2. Based on the different solidification structures of these layers, it is concluded that for the cellular layer the solidification front starts at the SiC surface. During growth of this layer Si is rejected, as EDX measurements do not indicate a significant amount of Si. In the case of the irregular reaction layer the solidification starts in the melt nearby the particle. The aforementioned results from the random orientation of the TiC grains. In addition this can be explained by the difference in melting temperature, which is higher for stoichiometric TiC (3067°C) than for SiC (2545°C). The presence of Ti_3SiC_2 might be explained by entrapped Si, which is in solution and cannot be rejected because of the solidified TiC grains. The solidification of the matrix corresponds to the triangle in the phase diagram formed by Ti, TiC_{1-x} and $Ti_5Si_3C_y$. The solidification route of the matrix can be explained quite easily because of the different solidification temperatures. The lower solidification temperature of the TiC dendrites in comparison with the TiC reaction layer stems from the lower carbon content as measured with EDX. Depending on the amount of Si in the liquid after solidification of TiC dendrites, solidification starts with nucleation of Ti grains or Ti_5Si_3. Finally, eutectic solidification takes place according to the Ti–Si phase diagram.

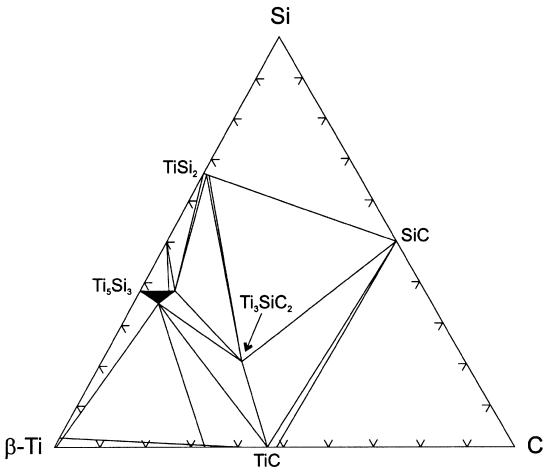

Fig. 11. Ternary phase diagram of Ti–Si–C. Isothermal section at 1200°C.

5. MECHANICAL PERFORMANCE

The mechanical performance of the MMC strongly depends on the properties of the interfacial region between the reinforcement and the matrix [14, 15]. A number of properties will be examined in more detail and possibly in correlation with the laser particle injection process. SiC particle injection into liquid Ti results in chemical reactions occurring at the interface, which might have detrimental consequences for the mechanical performance. Furthermore, high thermal stresses will be present in the modified layer, as the MMC is cooled down from high temperatures. These stress concentrations play an important role in damage initiation. Finally, hardness indentations are performed to initiate cracks in the matrix close to the reaction layer in order to study the crack initiation and propagation behaviour at the interface region.

The majority of MMCs are non-equilibrium systems due to the presence of a chemical potential gradient across the interface. This means that under certain conditions diffusion and/or chemical reactions will take place at the interface. These specific conditions concern the temperature and the interaction time. Under controlled circumstances the formation of a limited reaction layer might be desirable in order to obtain strong bonds. However, a thick reaction layer might detrimentally affect the composite properties. Therefore, it is extremely important to be aware of the influence of the process conditions in order to produce MMCs by means of a laser for practical applications. The most commonly used method to obtain a chemical bonding is by means of a diffusion welding process, while the layer thickness shows a parabolic dependence in time and can be estimated by $l \sim \sqrt{Dt}$ [16, 17]. In the literature it is reported that the mechanical properties of a diffusionally bonded Ti–SiC composite degrade for layer thicknesses above 1 μm [18]. However, this is not comparable with laser processing as the formation of the reaction layer mainly takes place when the matrix is in the liquid state. In principle this seems to be an uncontrollable situation also due to the convective flow in the meltpool. In particular the reaction of Ti with SiC exhibits a large thermodynamic driving force [19]. Nevertheless, it turned out to be feasible to minimize the reaction layer thickness by adjusting the particle injection position. If we compare the interaction time in diffusional processes with that of the laser embedding process, it differs by several orders of magnitude. For diffusional processes the interaction time is given in hours whereas in laser embedding it is given in seconds. If the length of the meltpool is 4 mm, the maximum time the SiC particles spend in the liquid Ti amounts to 0.44 s. By changing the injection position this interaction time will decrease.

The reaction layer thickness is found to decrease by changing the particle injection position towards the back of the laser beam in the negative x-direction, which is depicted in Fig. 12. The values are obtained by taking the average of at least ten reaction layer thicknesses in the middle of the track. The general tendency is that the reaction layer thickness decreases. So the different appearance of the reaction layer is related to the time the particles spent in the liquid titanium and the processing temperature. In principle the thin reaction layers are of the cellular type, whereas the irregular type is present for the thicker reaction layer. This transition

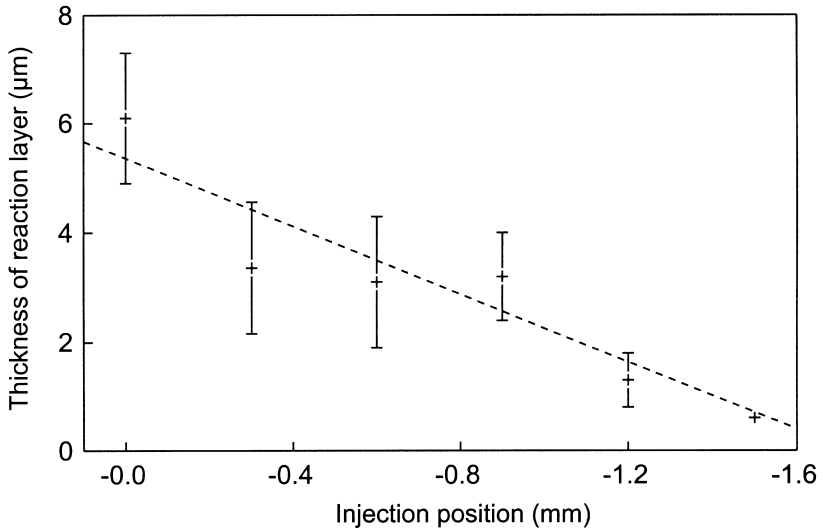

Fig. 12. Thickness of the reaction layer as a function of the injection position relative to the centre of the laser beam. (The dashed line only indicates the general decrease of the reaction layer thickness.)

takes place around a thickness of 2.5 μm, but it must be mentioned that this is certainly not a sharp transition.

In order to study the bonding between the TiC reaction layer and the SiC particle, hardness indentations are made to initiate crack formation in the matrix in the vicinity of the reaction layer. In the case of crack initiation, we examine the crack path through the reaction layer towards the SiC particle. The indents are obtained by means of a Vickers hardness tester with an applied load of 20 N. Although the applied force is constant, it must be mentioned that the crack propagation conditions all differ as far as the energy is concerned, due to the different matrix structures and the different distances between the pyramidal indent and the reaction layer. Besides the crack propagation behaviour these tests also reveal the crack initiation behaviour of the matrix material as the indents did not always result in crack formation.

Fracture of materials can be described, from an internal energy point of view, by the creation of free surfaces from bulk materials [20]. In the case of brittle materials, without stress concentrators or plastic deformation, this amounts to equating the release of strain energy to the energy required for creating free surfaces. The fracture toughness of SiC, TiC and TiN amounts to 2–5 MPa $m^{0.5}$, whereas the value of Ti–6Al–4V amounts to 55–120 MPa $m^{0.5}$.

The indents are made in the aforementioned set of laser tracks with six different particle injection positions, which resulted in two different types of reaction layers. In the case of the cellular reaction layer the initiated cracks are found to propagate straight ahead through the TiC reaction layer and to advance in the SiC particle without deflection at the interface, as can be seen in Fig. 13. This is an indication of a good load transfer at the interface. Furthermore, there is no clear crack path observed in the matrix, which could have been only plastically deformed. The irregular reaction layer exhibits the crack to follow the pores, as shown in Fig. 14. Two different phenomena are found to occur at the interface. In the first case, the crack traverses the interface without significant deflection. The second case shows the crack to deflect first along the interface followed by penetration into the SiC particle. The latter situation is shown in Fig. 15. The deflection can be partially explained by the presence of pores at the interface. However, in between the pores the SiC and TiC are still detached from each other, which indicates that the interface exhibits locally poor bonding. This might be explained by the different growth conditions as this type of reaction layer grows from the melt towards the SiC particle, possibly resulting in a weaker bond than the situation where the cellular reaction layer grows from the surface of the SiC particle. If we consider the crack initiation in the matrix, this is found to occur depending on the matrix structure. In the case of high dissolution of SiC, which implies the presence of thick reaction layers, the indents often initiated cracks in the matrix. On the other hand for limited dissolution of SiC, which implies thin reaction layers, the indents just occasionally initiated cracks. This is caused by the difference in yield stress of the microstructures. For regions containing large amounts of Ti_5Si_3 and TiC cracks are initiated more easily than for regions with Ti grains surrounded by eutectic structures. Therefore, the

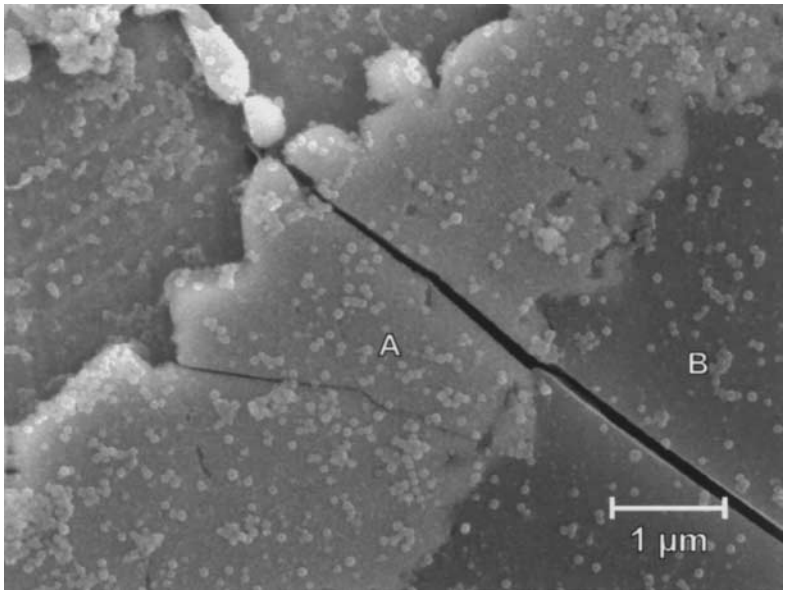

Fig. 13. SEM micrograph of a cellular reaction layer (A) showing crack propagation straight through the reaction layer of TiC into the SiC particle (B) without deflection at the interface.

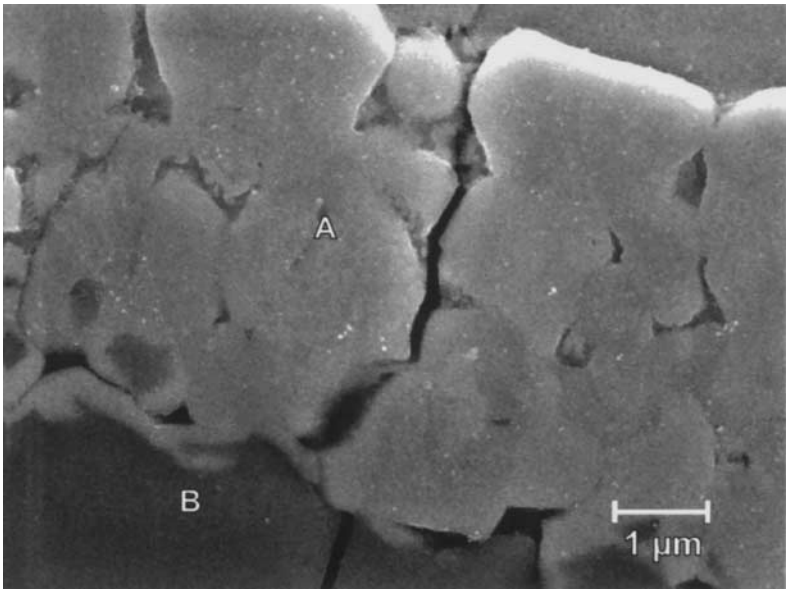

Fig. 14. SEM micrograph of an irregular reaction layer (A) showing crack propagation along the pores of TiC. At the interface the crack slightly deflects but finally propagates into the SiC particle (B).

latter matrix structure is favourable, due do its better capacity to relieve stress by plastic deformation.

6. CONCLUSIONS

The laser particle injection process appears to be very sensitive to the positioning of the powder injection, the interaction time of the particles with the laser and the amount of powder used. The possibility to change this in a controlled manner yields the possibility to vary the dissolution of the SiC particles and at the same time the composition of the matrix. The latter is very important because too much dissolution might result in a brittle matrix, which is undesirable with respect to the mechanical performance. In addition, the structure and properties of the reaction layer around the SiC particles changes for different injection positions. Crack formation induced by hardness indents indicates that the cellular reaction layer exhibits a better bond with the SiC particle than the irregular reaction layer. Experimental research presented in the literature indeed confirms that both materials might

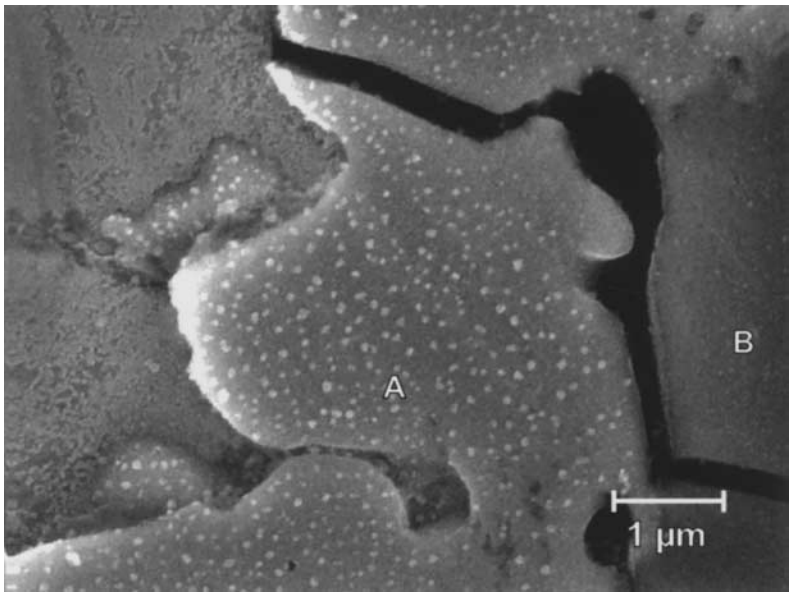

Fig. 15. SEM micrograph of an irregular reaction layer (A) showing crack deflection at the interface between TiC and SiC. Finally the cracks penetrate the SiC particle (B).

develop very strong bonds, which is important for the mechanical performance [21, 22].

Acknowledgements—The work is part of the research programme of IOP-Metalen (Den Haag) (IOP-C92617.RG.TN) and has been supported (in part) by the Foundation for Fundamental Research on Matter (FOM-Utrecht) and by the Netherlands Foundation for Technical Sciences (STW-Utrecht).

REFERENCES

1. Mridha, S. and Baker, T. N., *J. Mater. Proc. Technol.*, 1997, **63**, 432.
2. Abboud, J. H. and West, D. R. F., *J. Mater. Sci. Lett.*, 1991, **10**, 1149.
3. Ayers, J. D. and Tucker, T. R., *Thin Solid Films*, 1980, **73**, 201.
4. Abboud, J. H. and West, D. R. F., *J. Mater. Sci. Lett.*, 1992, **11**, 1675.
5. Baker, T. N., Xin, H., Hu, C. and Mridha, S., *Mater. Sci. Technol.*, 1994, **10**, 536.
6. Venables, J. A. and Harland, C. J., *Phil. Mag.*, 1973, **27**, 1193.
7. Loretto, M. H., *Electron Beam Analysis of Materials*. Chapman & Hall, London, 1994.
8. Rosenthal, D., *Trans. Am. Soc. Min. Engrs*, 1946, **11**, 849.
9. Abboud, J. H. and West, D. R. F., *Mater. Sci. Technol.*, 1989, **5**, 725.
10. Arunajatesan, S. and Carim, A. H., *Mater. Lett.*, 1994, **20**, 319.
11. Morgiel, J., Lis, J. and Pampuch, R., *Mater. Lett.*, 1996, **27**, 85.
12. Lis, J., Pampuch, R., Piekarczyk, J. and Stobierski, L., *Ceram. Int.*, 1993, **19**, 219.
13. Brukl, C. E., *Ternary Phase Equilibria in Transition Metal–Boron–Carbon–Silicon Systems* (VII). Springfield, IL, 1998.
14. Clyne, T. W. and Withers, P. J., *An Introduction to Metal Matrix Composites*. Cambridge University Press, London, 1993.
15. Chawla, K. K., in *Materials Science and Technology*, Vol. 13, ed. R. W. Cahn, P. Haasen and E. J. Kramer. VCH, Weinheim, 1993.
16. Warren, R. and Andersson, C. H., *Composites*, 1984, **15**(2), 101.
17. Martineau, P., Pailler, R., Lahaye, M. and Naslain, R., *J. Mater. Sci.*, 1984, **19**, 2749.
18. Reeves, A. J., Taylor, R. and Clyne, T. W., *Mater. Sci. Engng*, 1991, **A141**, 129.
19. Pan, Y. and Baptista, J. L., *J. Am. Ceram. Soc.*, 1996, **79**(8), 2017.
20. Broek, D., *Elementary Engineering Fracture Mechanics*. Noordhoff, Leyden, 1974, p. 257.
21. de Mestral, F. and Thevenot, F., in *The Physics and Chemistry of Carbides, Nitrides and Borides*, ed. R. Freer. Kluwer, Dordrecht, 1989.
22. Jiang, D. L., Li, Y. L. and Ma, L. T., *Mater. Sci. Engng*, 1989, **A109**, 401.